Journal of Marine Science and Application (2020) 19:101–115
https://doi.org/10.1007/s11804-020-00135-5

RESEARCH ARTICLE

A Numerical Investigation of Gap and Shape Effects on a 2D Plunger-Type Wave Maker

Amir H. Nikseresht [1,2] · Harry B. Bingham [1]

Received: 4 June 2019 / Accepted: 15 November 2019 / Published online: 30 June 2020

Abstract

The installation of plunger-type wave makers in experimental tanks will generally include a gap between the back of the wedge and the wall of the tank. In this study, we analyze the influence of this gap on the wave making performance of the plunger using two-dimensional (2D) CFD calculations for a range of nearly linear wave conditions and compare the results with both experimental measurements and linear potential flow theory. Three wedge-shaped profiles, all with the same submerged volume, are considered. Moreover, the generated waves are compared with the predictions of linear potential flow theory. The calculations are made using the commercial ANSYS FLUENT finite-volume code with dynamic meshes to solve the Navier–Stokes equations and the volume of fluid scheme to capture the air–water interface. Furthermore, the linear potential flow solution of Wu (J Hydraul Res 26:481–493, 1988) is extended to consider an arbitrary profile and serve as a reference solution. The amplitude ratios of the generated waves predicted by the CFD calculations compare well with the predictions of linear potential flow theory for a simple wedge, indicating that viscous effects do not influence this ratio for small-amplitude motions in 2D. By contrast, significant higher harmonic components are produced by larger amplitude motions. Also, the simple wedge is found to produce the smallest spurious higher harmonic content in the far-field wave.

Keywords Wave maker · Plunger-type · Berkeley wedge · Hyperbolic sine profile · Gap · Dynamic mesh · Volume of fluid

Article Highlights

- The influence of gaps between the tank wall and a wedge-shaped, plunger-type wave maker on the generated waves is investigated using 2D CFD calculations.
- To generate good quality waves, the gap behind the wedge should be as small as possible.
- Three wedge profiles are considered: a simple wedge, the Berkeley wedge profile, and a hyperbolic sine profile. The simple wedge is found to produce the smallest spurious higher harmonic content in the far-field wave.
- The average first harmonic amplitude generated by both the simple wedge and the Berkeley wedge profiles compare well with linear theory, while the hyperbolic sine profile does not.
- Higher harmonic component generation is observed to increase more rapidly with increasing stroke amplitude for the Berkeley wedge than for the simple wedge.

✉ Amir H. Nikseresht
nikser@sutech.ac.ir

[1] Department of Mechanical Engineering, Technical University of Denmark, DK-2800 Kgs Lyngby, Denmark

[2] Department of Mechanical Engineering, Shiraz University of Technology, Shiraz 71555-13876, Iran

1 Introduction

Three basic types of wave makers (i.e., piston, flap, and plunger types) are used in laboratories. The most commonly used type of wave maker is the piston type, which generates waves through oscillatory motion in the direction of wave propagation. Most of the published studies based on viscous flow solvers have focused on either piston-type or flap-type wave makers (Higuera et al., 2015; Prasada et al., 2017; Dao et al., 2018; Martínez-Ferrer et al., 2018). However, plunger-type devices, where a floating body is oscillated vertically, are also often used to generate waves in experimental facilities. In contrast to piston-type and flap-type wave makers, analytical solutions are unavailable for the plunger-type wave maker. However, a number of numerical solutions based on both linear potential flow theory and the Navier–Stokes equations have been presented in the literature. Linear solutions via eigenfunction expansion were obtained by Wang (1974) and Wu (1988). Two-dimensional (2D) linear numerical solutions were also obtained by Wu (1991) using the boundary element method (BEM) and by Arcari (2015) using the finite difference method. Nonlinear BEM solutions, which showed good

consistency with the experimental measurements, were obtained by Kashiwagi (1996) and Koo and Kim (2006). Mikkola (2006, 2007) used a finite-volume Navier–Stokes solver but neglected viscous effects. Yim et al. (2008) validated a RANS model by comparing the numerical results with the experimental data involving wave generation by dropping a rigid body at various heights into a 2D flume partially filled with water. Elangovan and Lal (2008), Lal and Elangovan (2008), and Gadelho et al. (2015) solved the Navier–Stokes equations for a triangular plunger-type wave maker. Yeung and Jiang (2014) investigated the shape effects on the viscous damping and motion of a heaving cylinder using the random vortex method. Madhi et al. (2014) applied both nonlinear and viscous potential flow solutions using the random vortex method to the "Berkeley wedge" profile and compared the results with experimental measurements. Azadian-Kharenjani et al. (2018) applied a nonlinear viscous flow solver to investigate the effect of wedge angle (with volume held constant) on the generated wave quality.

In all of the aforementioned studies, the wedge was either placed far from the tank wall or sliding along the wall without a gap between the back of the wedge and the tank wall. For most real installations, there is a finite gap between the wedge and the tank wall. One of the goals of this study is to consider the effect of this finite gap on the resultant wave. We also investigate the performance of two alternative profiles compared with that of the simple wedge. Calculations are made using the ANSYS FLUENT 16 CFD software with dynamic grids near the moving wedge and the volume of fluid (VOF) scheme to capture the air–water interface. A series of small-amplitude conditions (wave height divided by wavelength less than approximately 0.03) are run, and the results are compared with the linear potential flow theory and experimental measurements.

2 Description of the Wave Maker

In Figure 1, a 2D section of the Technical University of Denmark (DTU) flume with the wedge wave maker is shown.

The flume at DTU where the experiments were performed is 28-m long × 0.6-m wide and 0.8-m deep. The dimensions of the wedge have been selected on the basis of two constraints. First, the device has to generate waves whose amplitudes approach the breaking wave limit. The Battjes breaking wave criteria for deep-water waves state that the maximum height of a stable wave H_{max} is a function of the wavelength λ: $H_{max} = 0.14\lambda$ (Arcari, 2015). As the first constraint, all breaking wave conditions should remain inside the tank for the target range of wave periods T. As the second constraint, all breaking wave conditions should generate intermediate-water and deep-water waves,

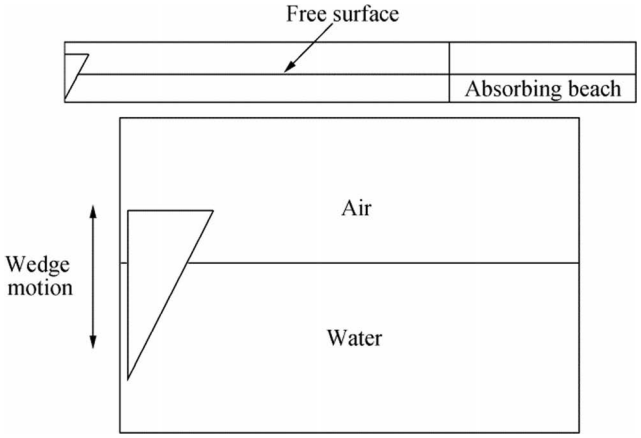

Figure 1 2D section of the wedge wave maker in the Technical University of Denmark (DTU) flume

which means $\frac{2\pi h}{gT^2} \geq 0.05$, (Arcari, 2015) where h is the water depth and g is the gravitational acceleration.

With the aforementioned constraints, the water depth is set to 0.65 m, the draft of the wedge is fixed to $D = 0.45$ m, and the clearance value, which is equivalent to the maximum stroke amplitude, is $S_{max} = 0.2$ m. Finally, on the basis of the initial study of (Arcari, 2015), the wedge breadth at the free surface is set to $b = 0.225$ m. Table 1 summarizes the limits of the preliminary parameters of the wedge and waves. The values h, b, D, and S_{max} are kept constant throughout the study. λ_{max} and λ_{min} are the wavelengths of the longest and shortest target frequencies, respectively. The target frequencies cover an interval of intermediate-water and deep-water waves for this tank.

Given that the wedge fills the entire width of the flume, a 2D analysis was performed. Moreover, 2D wave theory has been used to design the wedge and wedge motion (Arcari, 2015).

As this problem is a dynamic problem, the mesh should be changed on the basis of the motion of the wedge. Therefore, a dynamic mesh, which can be regenerated at each time step, is used. To test the wedge under nearly linear wave conditions, the frequency range of 4–12 rad/s is selected. The characteristics of the waves and stroke amplitudes are shown in Table 2.

We will compare our calculations for these conditions with the predictions of linear potential flow theory by considering the ratio A/S, where $A = H/2$ is the far-field amplitude of the generated wave at frequency ω. Possible nonlinear effects will be identified through nonzero amplitude components at multiples of the fundamental frequency.

Table 1 Preliminary parameters of the wedge and waves (Arcari, 2015); unit, m

h	b	D	S_{max}	H_{max}	λ_{max}	λ_{min}
0.65	0.225	0.45	0.2	0.28	3.06	0.5

Table 2 Test wave conditions

Test case No.	T (s)	ω (rad/s)	λ (m)	$2S$ (m)	$\left(\frac{H}{\lambda}\right)_{\text{Linear theory}}$
1	0.57	11.023	0.5	0.007	0.0177
2	0.70	8.976	0.76	0.007	0.01033
3	0.83	7.57	1.08	0.007	6.38e-3
4	0.97	6.477	1.45	0.047	0.02738
5	1.10	5.712	1.84	0.047	0.0185
6	1.23	5.108	2.25	0.047	0.0129
7	1.37	4.586	2.65	0.087	0.01756
8	1.50	4.1887	3.06	0.127	0.0198

3 Mathematical Modeling

The selected range of wave conditions is in the intermediate-water to deep-water regime where we expect viscosity and turbulence to be of importance only in the vicinity of the wedge. The maximum Reynolds (*Re*) numbers based on the maximum velocity of the wedge in test case 8 ($S\times\omega =$ 0.266 m/s) with characteristic lengths of $2S$ and b are 16 809 and 66 177, respectively. Comparing these with the critical *Re* number of a flat plate (5 × 10e5) (Cengel and Cimbala, 2006), it is clear that all *Re* numbers are less than the critical value. Therefore, the flow field around the wedge is assumed to be laminar. Given that the flow is assumed to be incompressible laminar flow, the continuity and momentum equations are expressed as follows:

$$\nabla \cdot V = 0 \tag{1}$$

$$\frac{\partial V}{\partial t} + (\mathrm{V} \cdot \nabla)V = -\frac{1}{\rho}\nabla p + \frac{1}{\rho}\nabla \cdot \left(2\mu\overline{D}\right) + g \tag{2}$$

where $\overline{D}$ is the stress tensor rate with the components:

$$D_{ij} = \frac{1}{2}\left(\frac{\partial V_i}{\partial X_j} + \frac{\partial V_j}{\partial X_i}\right) \tag{3}$$

and p, μ, V, and ρ are the pressure, dynamic viscosity, fluid velocity vector, and fluid density, respectively.

Note that the dynamic condition, i.e., continuity of pressure at the interface, is automatically implemented by the VOF method. The kinematic condition, which states that the interface undergoes convection in fluid, can be expressed in terms of the volume fraction φ as follows (Nikseresht et al., 2008):

$$\frac{\mathrm{D}\varphi}{\mathrm{D}t} = \frac{\partial \varphi}{\partial t} + (V \cdot \nabla)\varphi = 0 \tag{4}$$

where φ is a color function with a magnitude between 0 and 1 (more explanation is presented in the "Computational schemes" section).

The motion of the wave maker mentioned previously (Wu, 1988) can be expressed as follows:

$$Y(t) = S\sin\omega t \tag{5}$$

$$V(t) = S\omega\cos\omega t \tag{6}$$

$$\omega^2 = gk\tanh kh \tag{7}$$

In Eqs. (5) and (6), the terms Y, V, and S represent the vertical displacement, velocity, and stroke amplitude of the wave maker, respectively. The radian frequency of oscillation is ω, and Eq. (7) expresses the linear dispersion relation relating the frequency and the wave number $k = 2\pi/\lambda$.

4 Numerical Procedure

In the present study, the commercial ANSYS FLUENT finite-volume code is used to solve the Navier–Stokes equations for the simulation of the flow field around the moving wedge and in the flume. A second-order upwind scheme is used to discretize the convective terms in the momentum equations, and the SIMPLE algorithm is used to couple the pressure-based and velocity-based equations. An explicit VOF scheme is also used to capture the interface in a two-phase flow. A dynamic mesh scheme is used for the moving region. The UDF program is used to control the wave maker velocity and stroke using Eqs. (5) and (6). For the absorption of waves, a numerical beach is applied over the last 8 m of the flume.

4.1 VOF Scheme

In the VOF method with the geo-reconstruct scheme (Nikseresht et al., 2005, 2009), the interface is described implicitly, and the data structure that represents the interface is the fraction φ of each cell that is filled with the reference phase, i.e., phase 1. The scalar field φ is often referred to as the color function. The magnitude of φ in the cells cut by the free surface is between 0 and 1 ($0 < \varphi < 1$) and away from it is either 0 or 1.

μ and ρ in any cell (denoted by subscript ij) can be computed using φ by simply taking the volume average over the cell as follows:

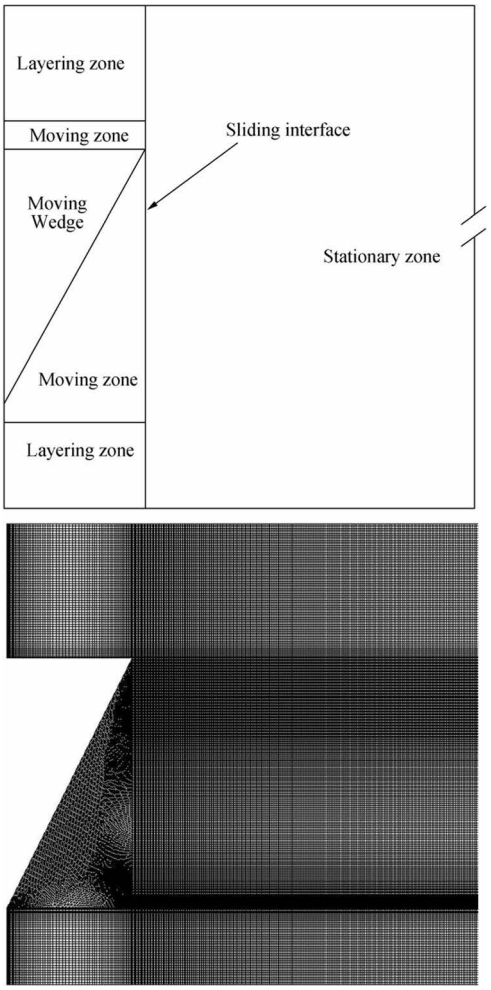

Figure 2 Zones and mesh system around the wedge

$$\rho_{ij} = \varphi_{ij}\rho_L + \left(1-\varphi_{ij}\right)\rho_a \tag{8}$$

$$\mu_{ij} = \varphi_{ij}\mu_L + \left(1-\varphi_{ij}\right)\mu_a \tag{9}$$

where subscripts L and a denote liquid and air, respectively.

The data of φ are given at the beginning of the computational cycle. However, no approximation of the interface position is known. Finding the interface is implicit because one needs to invert the data of φ to determine the approximate interface position. In other words, an algorithm for interface reconstruction is needed (Nikseresht et al., 2009).

4.2 Dynamic Mesh Update

A dynamic mesh layering and a sliding mesh are used to regenerate the mesh in the dynamic zone. These schemes are explained briefly as follows:

In the dynamic mesh layering method, dynamic layering of prismatic (hexahedral and/or wedge) mesh zones can be utilized to add or remove layers of cells adjacent to a moving boundary on the basis of the height of the layer adjacent to the moving surface. The layer of cells adjacent to the moving boundary is split into two layers or merged with the layer of cells next to it on the basis of the height of the cells.

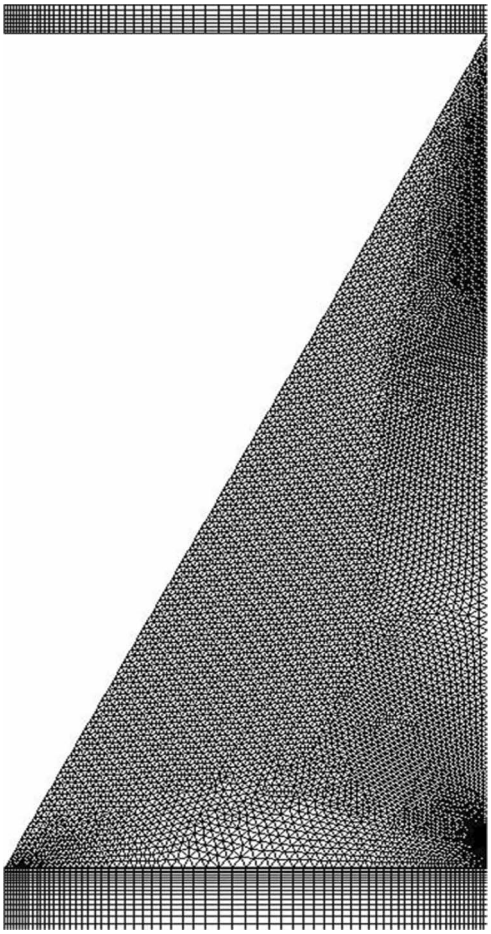

Figure 3 Close-up of the moving and sliding mesh regions

In the sliding mesh method, two or more cell zones are used. Each cell zone is bounded by at least one "interface zone" where it meets the opposing cell zone. The interface zones between adjacent cell zones are associated with one another to form a "grid interface." These two cell zones will move relative to each other along the grid interface. The cell zones slide, i.e., rotate or translate, relative to each other along the grid interface in discrete steps during the calculation.

4.3 Mesh Generation and Grid Independence Check

We first consider the case where there is no gap between the wedge and the wall of the tank. The domain depicted in Figure 2 is divided into three regions, a moving zone with both structured and unstructured meshes that moves along with the wedge, a dynamic layering zone above and below the moving zone with a structured mesh, and a stationary zone far from the wedge with a structured mesh. Moreover, there is

Table 3 Grid independence check

Case No.	Mesh system	Nodes per wavelength	Nodes per wave height	Amplitude ratio	Percentage of difference	Total grid No.	Time consumption (s) for 1 T on 16 cores (Xeon-E5-2660-V3)
1	1	50	7	1.2285		489 547	4900
1	2	100	11	1.27	4.4	839 621	7000
1	3	150	11	1.275	0.39	1 161 367	8000
1	4	200	15	1.278	0.234	1 575 711	14 000

an interface between stationary and moving zones. Layering and sliding mesh schemes are used in the dynamic layering zone and the interface, respectively. A close-up of the mesh near the wedge with the moving zone is shown in Figure 3. This entire mesh system moves with the wedge. After establishing a suitable mesh system, we confirm the mesh independence of the calculations for test case 1 in a real installation with a 1 cm gap to determine the number of nodes that is sufficient to obtain a good result for each wave number or frequency. The A/S ratio (where A is the wave amplitude and S is half of the stroke length) for the generated wave is calculated after 50 time periods to enable the domain to reach a steady state. Harmonic analysis of the computed wave elevation signals over three wavelengths starting from a distance of $x = 2h$ from the wedge where the evanescent mode effects are negligible (Keaney et al., 2014) is conducted via least squares fitting to a sum of sinusoids at the fundamental frequency and its first four higher harmonic components. The value A represents the average fundamental harmonic amplitude over the test region. Possible nonlinear effects can be evaluated through the amplitudes of the higher harmonic components. The results are shown in Table 3 for different grid resolutions. Notably, no significant changes in the A/S ratio for different resolutions are observed. Therefore, we conclude that at least 100 grid points per wavelength and 11 grid points per wave height are a good mesh resolution for all calculations.

Figure 4 shows the wave elevation versus position for test case 7 with 100 nodes per wavelength (t7-Lambda = 100) and 200 nodes per wavelength (t7-Lambda = 200), and the results of the two calculations are consistent.

5 Comparison With Linear Potential Flow Theory Without a Gap

To validate the proposed method and schemes, the present results without a gap are compared with linear potential flow solutions obtained using the semi-analytical method of Wu (1988) and the numerical solutions obtained using the OceanWave3D (OW3D) finite difference method solver (Hicks, 2017). The average A/S ratio for the three solutions is plotted versus the wave angular frequency in Figure 5 and tabulated in Table 4. The present A/S ratios show a maximum difference of 4% compared with the linear theory. Therefore, the results are consistent with this theory. The theoretical wave elevation versus the position in test case 5 is compared with the present calculations shown in Figure 6 which also shows good consistency.

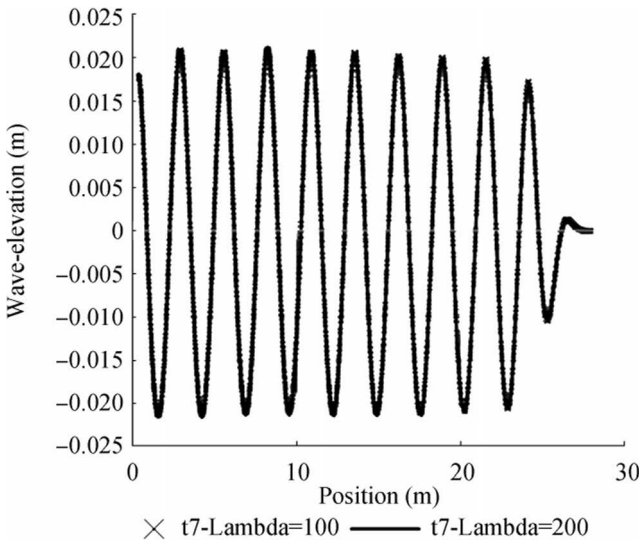

Figure 4 Grid independence at angular frequency of 4.587

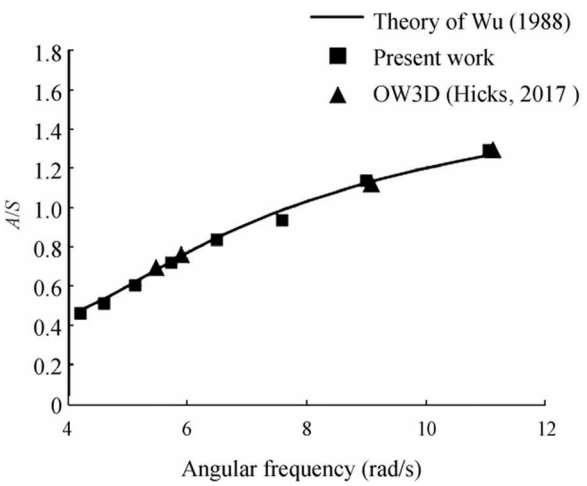

Figure 5 Comparison of the wave amplitude to stroke amplitude ratio in the present work with the linear theory of Wu (1988) and OW3D (Hicks, 2017)

Table 4 Comparison of the amplitude ratios in the present work with the theory of Wu (1988)

Case No.	T (s)	λ (m)	Steepness, Wu (1988)	Steepness, present work	Amplitude ratio, Wu (1988)	Amplitude ratio, present work	% difference of the amplitude ratio
1	0.57	0.5	0.0177	0.01714	1.265	1.29	2.0
2	0.7	0.76	0.1033	0.01039	1.122	1.1492	2.42
3	0.83	1.08	6.38e-3	0.00614	0.985	0.944	4.16
4	0.97	1.45	0.02738	0.266	0.845	0.839	0.71
5	1.10	1.84	0.0185	0.0183	0.724	0.727	0.41
6	1.23	2.25	0.0129	0.01286	0.6217	0.6215	0.032
7	1.37	2.65	0.01756	0.01665	0.535	0.5294	1.046
8	1.50	3.06	0.0198	0.01924	0.47688	0.4672	2.02

6 Effect of the Gap Behind the Wedge

We now investigate the effect of the gap between the flume wall and the back of the wedge on the performance of the wave maker. Therefore, the 1 cm gap located at the back of the wedge is divided into 3, 6, and 20 parts to ensure a grid-independent result when including this region. Changing the resolution of the mesh shows only a slight effect on the wave elevation. Table 5 shows the comparison of the A/S ratio of the wedge with and without a gap in all test cases and indicates that the maximum difference of the A/S ratio is approximately 3%. Figure 7 also includes the experimental results of Hicks (2017). These experimental results were obtained in a narrow flume with a width of 0.6 m. Figure 7 shows that the results are consistent with the experimental measurements at low frequencies but begin to deviate at high frequencies where they instead become consistent with the potential flow calculations. We assume that this discrepancy at high frequencies is due to 3D effects, in particular the energy loss due to vorticity generation in the small gaps between the ends of the wedge and the side walls. 3D calculations currently in progress should provide evidence to either support or refute this supposition.

To better understand the flow in the gap, we consider the velocity vector of test case 6 for the mesh with the highest resolution and a period of $T = 1.23$ s. The region near the bottom of the wedge, at four instances of time over one period, is shown in Figures 8 and 9. Although the vorticity magnitude at the bottom region of the wedge with a gap is relatively higher than that of the wedge without a gap, this does not reduce the energy of the generated wave, as the wave height is the same with and without a gap. Given that both of these calculations are also quite consistent with the predictions of linear potential flow theory, we can conclude that the narrow gap does not extract energy from the generated wave. This finding indicates that the energy required to

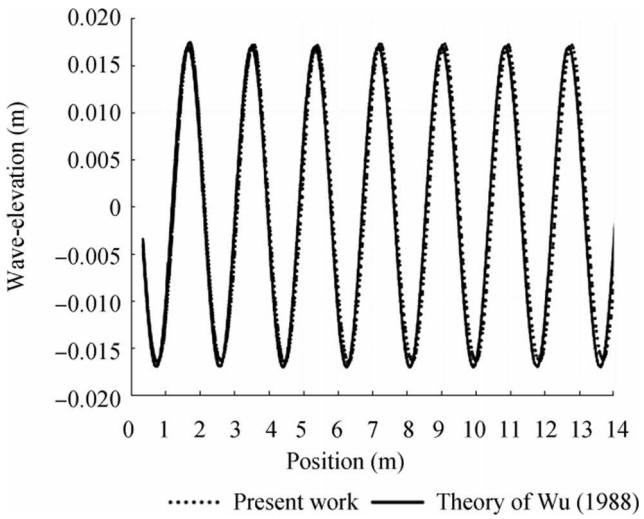

Figure 6 Comparison of the wave elevation in the present work with the linear theory of Wu (1988) for a wave angular frequency of 5.712

Table 5 Comparison of the wave amplitude ratio for the wedge with and without a gap

Case No.	T (s)	λ (m)	Wave amplitude ratio of the wedge with a 1 cm gap	Wave amplitude ratio of the wedge without a gap	Percent of wave height increase
1	0.57	0.5	1.27	1.29	1.57
2	0.7	0.76	1.1354	1.1492	1.215
3	0.83	1.08	0.9344	0.944	1.027
4	0.97	1.45	0.836	0.839	0.36
5	1.10	1.84	0.719	0.727	1.112
6	1.23	2.25	0.6114	0.6215	1.652
7	1.37	2.65	0.5111	0.5294	3.6
8	1.50	3.06	0.462	0.4672	1.126

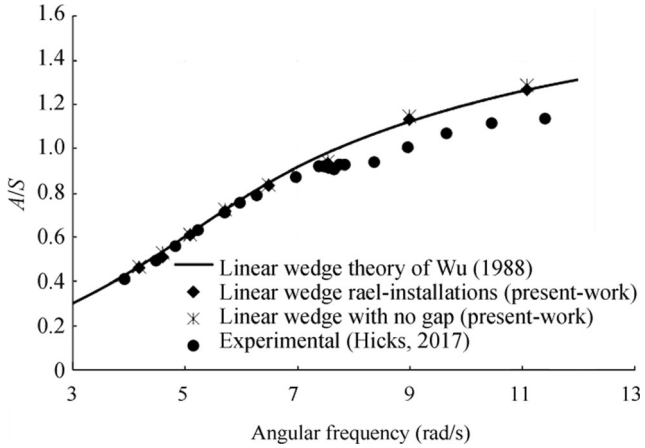

Figure 7 Comparison of the wave amplitude to stroke amplitude ratio in the present work with a 1 cm gap (real installations) and without a gap behind the wedge with the linear theory of Wu (1988) and the experimental measurements (Hicks, 2017)

generate the vorticity comes from a slight increase in the required force applied to the wedge.

We also consider the effect of increasing the size of the gap between the wedge and the wall to 50 cm. Figure 10 shows the wave elevation in front of the wave maker for test case 2 (high angular frequency) and test case 6 (moderate angular frequency). The difference between the generated wave heights with and without a large gap is approximately 3.5% in test case 2 and 12.5% in test case 8. Clearly, a large gap enables the leakage of wave energy behind the wedge, and this leakage increases with the increase in the wavelength. For high-frequency wedge motions, the generated wave behind the wedge has a small amplitude. However, for long waves (low frequency), the wave behind the wedge becomes significant and has a considerable effect on the generated wave.

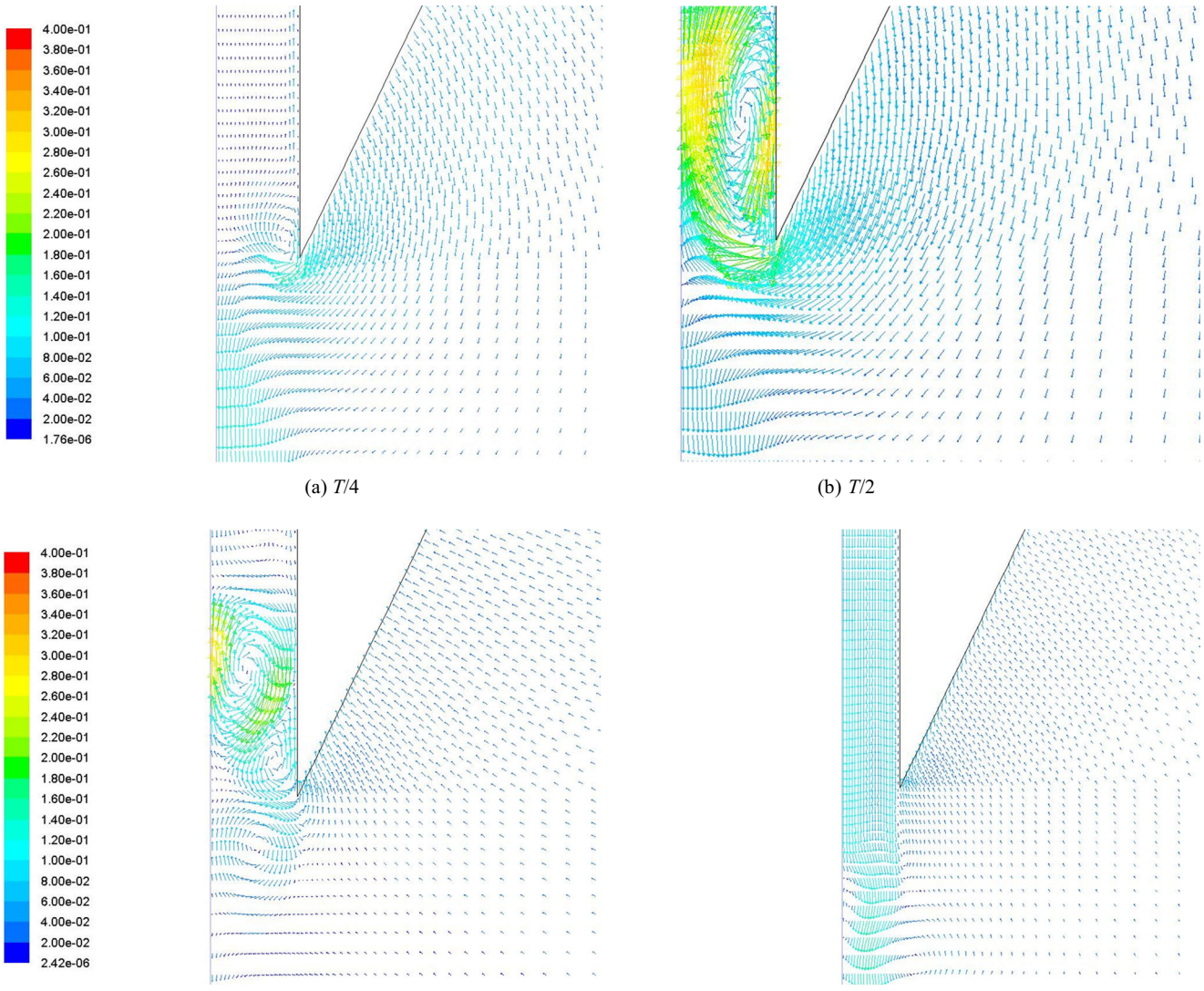

Figure 8 Velocity vector (m/s) at four instances of time over one period after 30 s ($T = 1.23$ s).

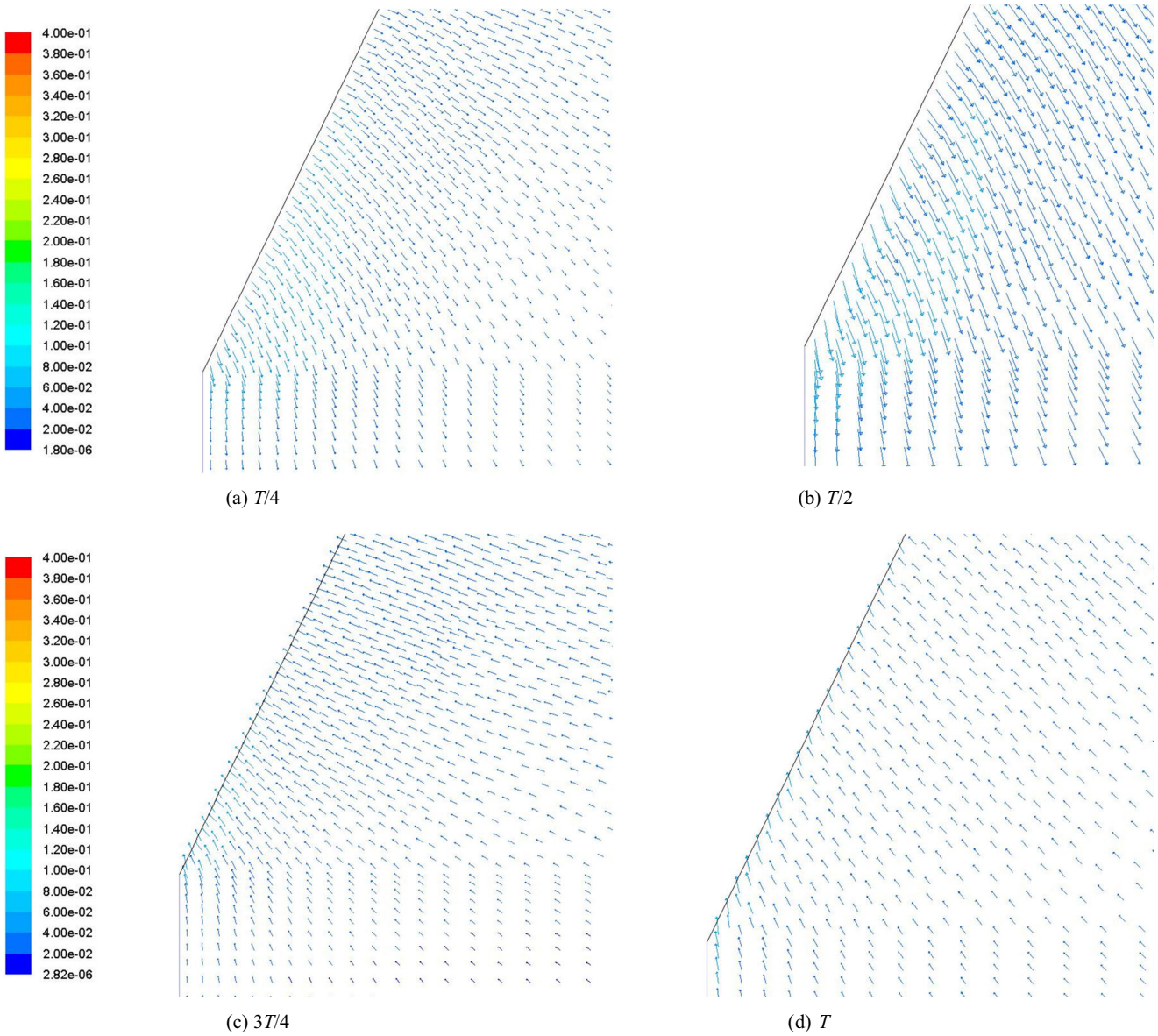

Figure 9 Velocity vector (m/s) at four instances of time over one period after 30 s for the wedge without a gap ($T = 1.23$ s)

Figure 11 shows an envelope plot of the surface elevation both behind and in front of the wedge for test case 4. Notably, the 0 value in the x-axis indicates that the starting point of the gap and the wedge position is between 0 and 0.25 on the x-axis. From this, we observe that significant motion is induced in the gap, which appears to consist mostly of the piston mode at the forcing frequency together with the first sloshing mode in the gap. This leads to significant irregularity in the wave generated in front of the wedge, which is depicted in Figure 12. This is clearly an important nonlinear phenomenon, which needs further investigation to be fully understood, but it shows the importance of keeping the gap behind the wedge as small as possible.

7 Effect of Wedge Shape

In this section, the effect of wedge shape on the generation of the wave is investigated. Three different 2D geometries as possible shapes for the floating body are shown in Figure 13.

In all wedges, the initial submerged volume should be the same, and the draft of the wedge D is set equal to 0.45 m. In terms of these two fixed parameters, the hyperbolic sine curve wedge is defined as follows:

$$X(y) = \frac{b_0 \sinh(a(y+D))}{\sinh(aD)}$$
$$b_0 = \frac{\Delta\, a \sinh(aD)}{(\cosh(aD)-1)} \tag{10}$$

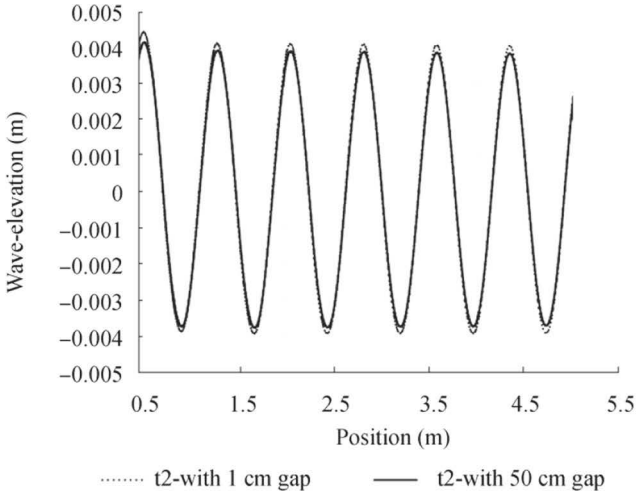

(a) With an angular frequency of 8.976

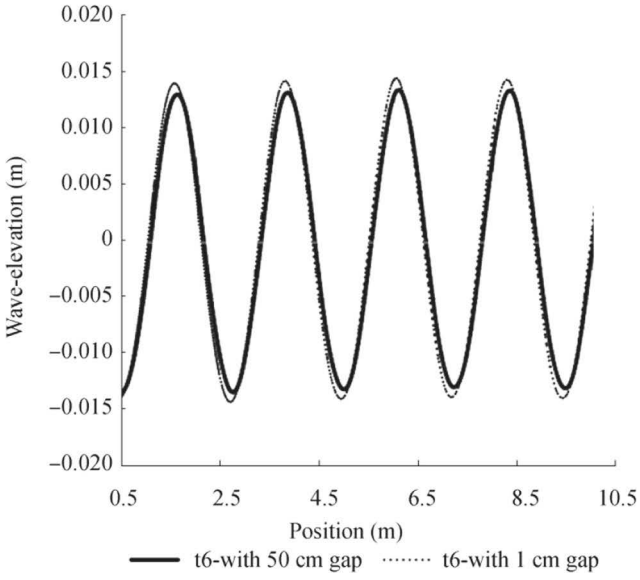

(b) With an angular frequency of 5.108

Figure 10 Comparison of wave height with different gaps behind the wedge

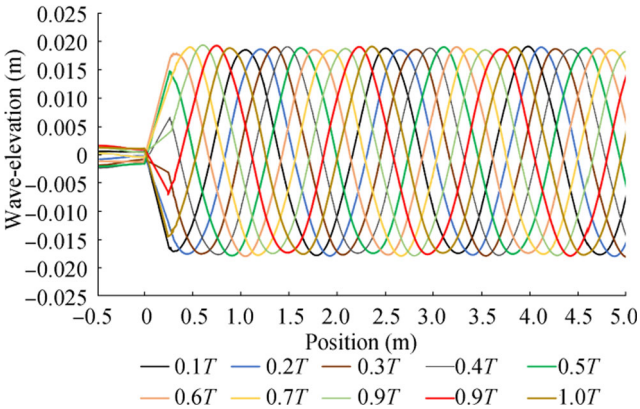

Figure 11 Envelope plot of the surface elevation both behind and in front of the wedge for test case 4

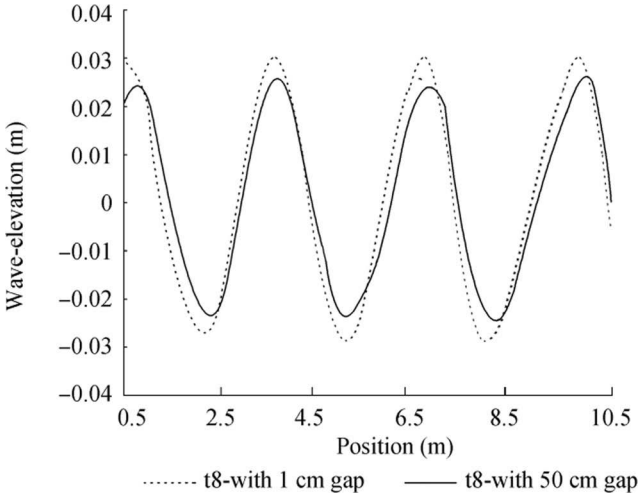

Figure 12 Comparison of wave shapes with different gaps behind the wedge for an angular frequency of 4.188

where Δ is the initial submerged volume of the triangular wedge and $a = \frac{\pi}{D}$.

Similarly, the Berkeley wedge (Madhi et al., 2014) is defined as follows:

$$X(y) = b_B\left(A\left(\frac{y+D}{D}\right)^2 + B\left(\frac{y+D}{D}\right)^3 + C\left(\frac{y+D}{D}\right)^4\right)$$
$$A = 3 + C, B = -2-2C, C = \frac{(3+6d_*)}{\left(6(d_*+1)^2-6\,d_*-5\right)} \tag{11}$$

where b_B is the beam that has the same volume as the triangular wedge and $d_* = -0.335$.

The two new wedges are sketched in the Gambit software, and a mesh with approximately the same resolution as the triangular wedge is generated, as shown in

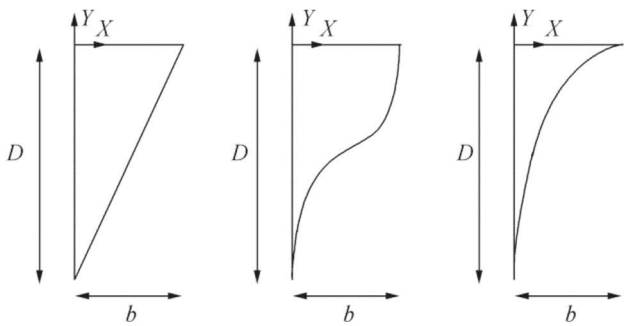

(a) Triangular wedge (b) Berkeley wedge (c) Hyperbolic sine curve wedge

Figure 13 Three different wedge shapes for wave generation

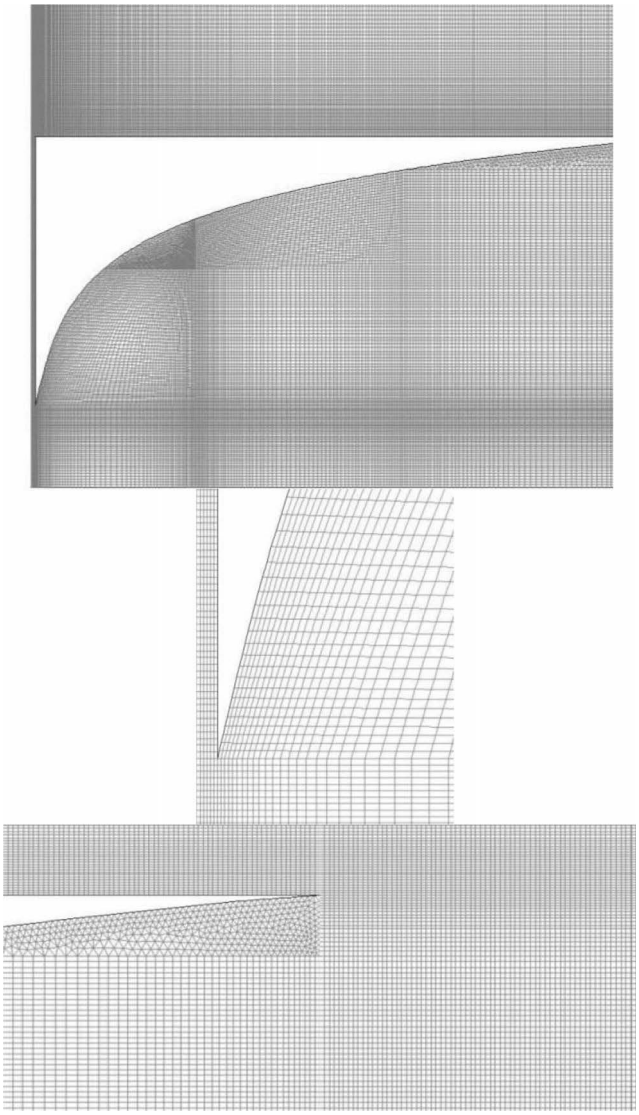

Figure 14 Generated mesh around the hyperbolic sine wedge

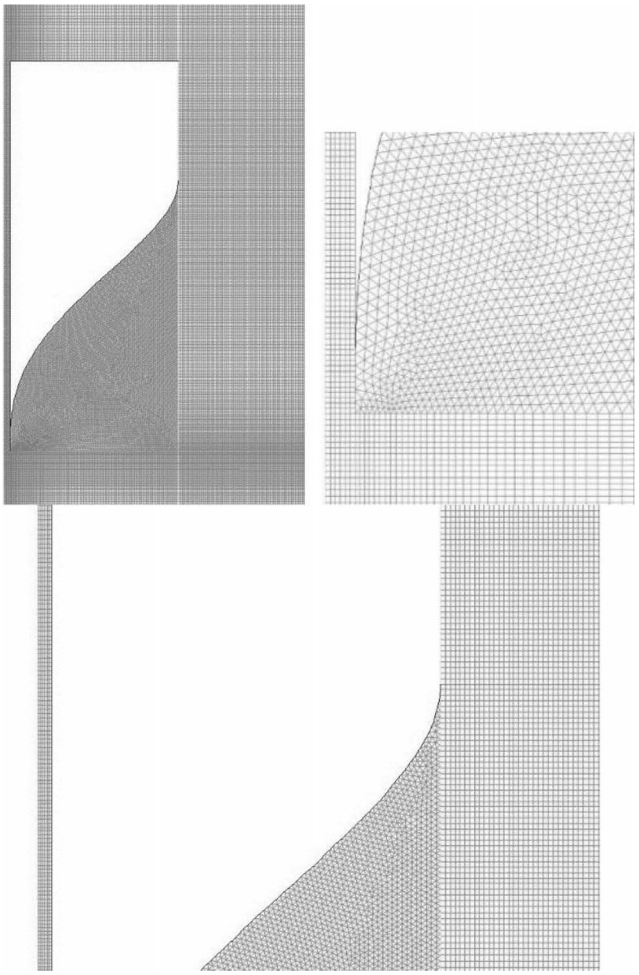

Figure 15 Generated mesh around the Berkeley wedge

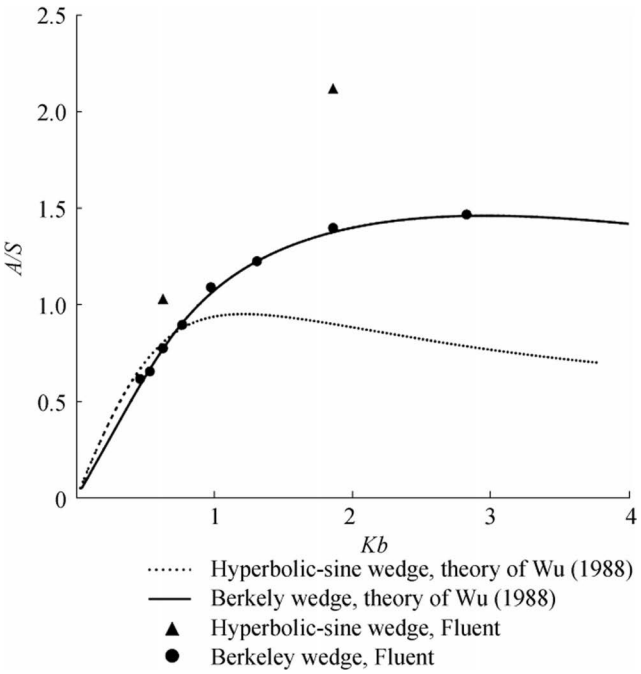

Figure 16 Comparison of theory of Wu (1988) with the present work for the hyperbolic sine and Berkeley wedges

Figures 14 and 15. In this part, only test cases 2 and 6, i.e., one high-frequency case and one low frequency case, respectively, were solved using the two new wedges. The computed A/S ratio is compared with the value predicted by the potential flow modal expansion method of Wu (1988), which has been extended to solve for arbitrary body shapes (Fig. 16). Figure 16 shows a good consistency between the average amplitude ratio of the wave generated by the Berkeley wedge and the potential flow result. In the case of the hyperbolic sine wedge, high-amplitude waves are generated, which do not match the linear theory at all.

Figures 17 and 18 show the wave elevation versus position for the two wedges in test case 6. In both cases, some irregularities in the waves are observed. However, the shape of the waves for the Berkeley wedge is better

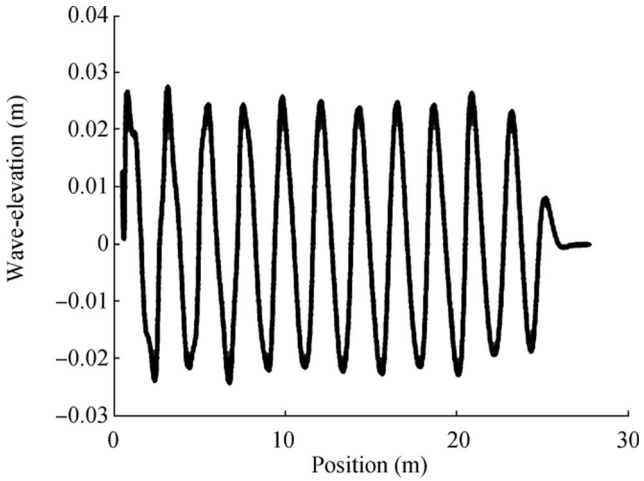

Figure 17 Wave elevation versus position for the hyperbolic sine wedge in test case 6

than that for the hyperbolic sine wedge. To further investigate the flow field, the velocity vectors in both cases are shown in Figure 19 for test case 6. Notably, for the hyperbolic sine shape, the velocity profile in the air region between the free surface and the wedge is complex, and some large vortices are generated with the velocity of the air near the free surface reaching nearly 6.5 m/s. This evidently has a strong effect on the shape of the wave. For the Berkeley wedge, the maximum velocity of the air is approximately 0.6 m/s, which does not affect the free

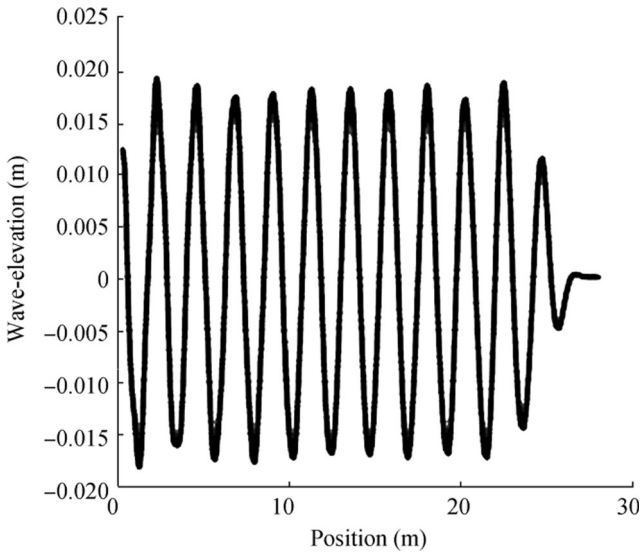

Figure 18 Wave elevation versus position for the Berkeley wedge in test case 6

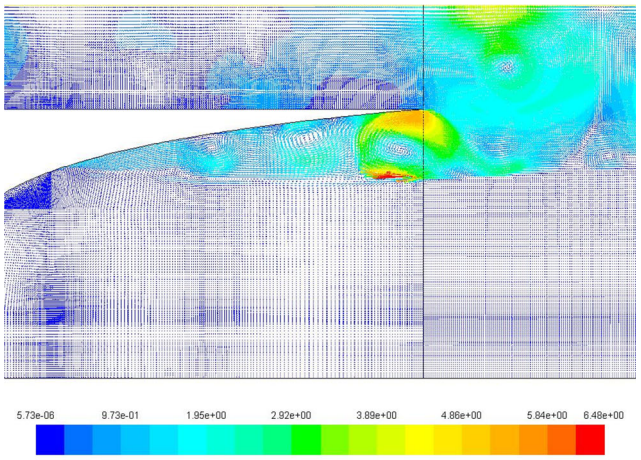

(a) Hyperbolic sine wedge

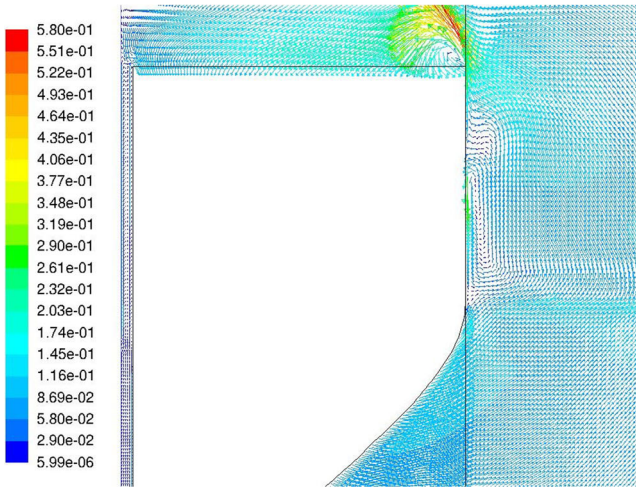

(b) Berkeley wedge

Figure 19 Velocity vectors on the free surface for different wedge wave makers in test case 6

surface shape. Evidently, estimating the A/S ratio and deriving a transfer function for the hyperbolic sine wedge are difficult tasks. The high gradient of the profile at the intersection with the free surface produced by this shape does not seem to be a good choice for such a wave maker.

For a closer investigation of the flow field in the gap behind each wedge, the velocity vector at the bottom region of the wedges at four instances of time over one period are sketched in Figures 20 and 21 for test case 6 with the time period of $T =$ 1.23 s. Although the velocity profile is more complex at the bottom region of the Berkeley wedge than that of the triangular wedge, it can be observed that, for both Berkeley wedge and hyperbolic sine wedge (as well as for the triangular

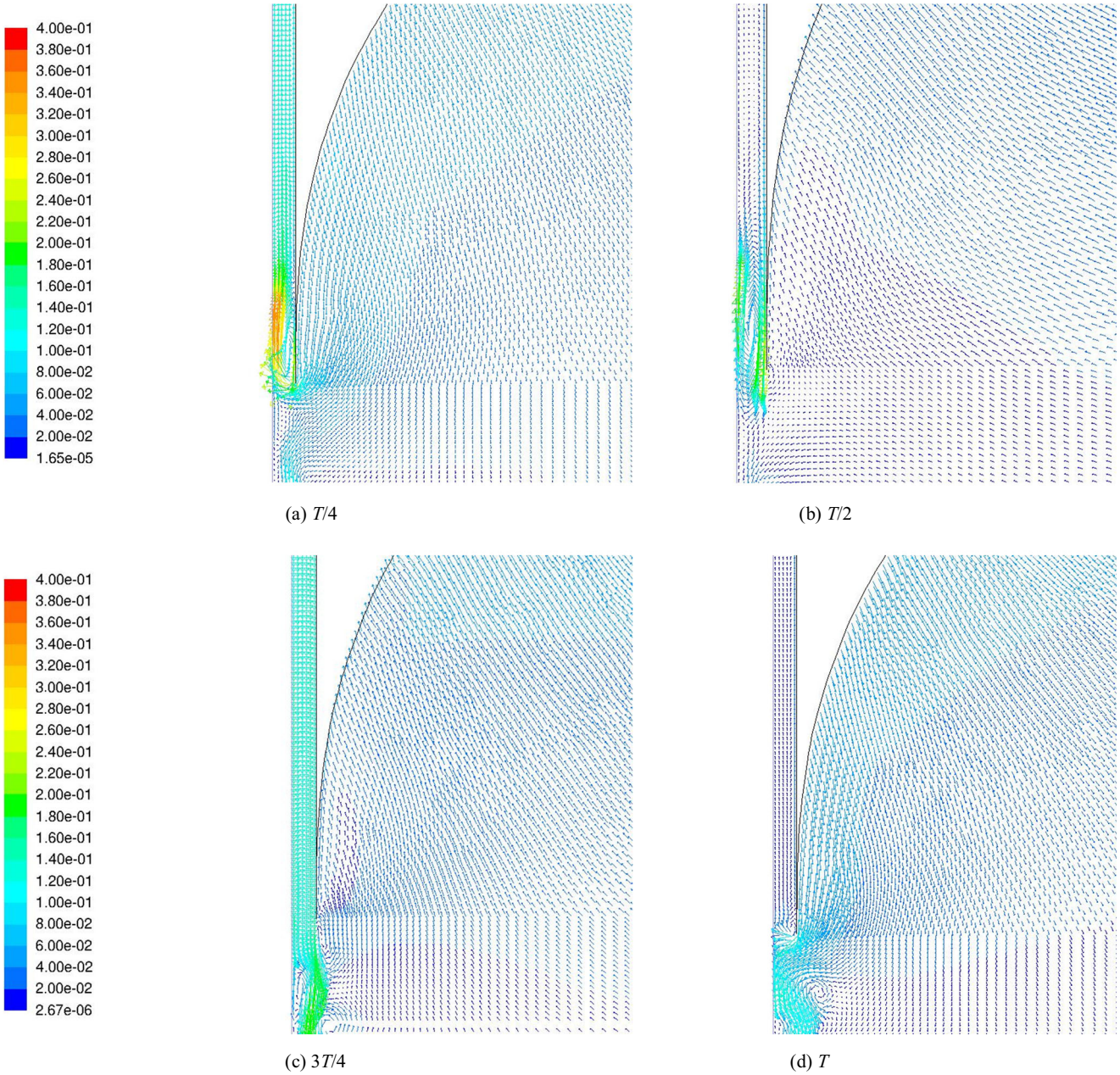

Figure 20 Velocity vector (m/s) for test case 6 at four instances of time over one period after 30 s for the Berkeley wedge

wedge), the flow in the gap has no significant effect on the far-field wave height.

For the triangular wedge, the same test cases (Table 2) were run again with the Berkeley wedge wave maker. The first harmonic A/S ratio is calculated and compared with the results of linear potential flow theory shown in Figure 16. Compared with the results for the simple wedge, more significant higher harmonic components were detected in the waves generated by the Berkeley wedge at lower frequencies with nonlinearity that is slightly higher than that at higher frequencies (see Table 2). One example of this is shown in Figures 22 and 23. To extract the harmonic amplitudes, we performed least squares fitting to a steady-state portion of the time series at three locations, i.e., $x = 5$, 10, and 15 m. Fitting is performed using the sum of the sine and

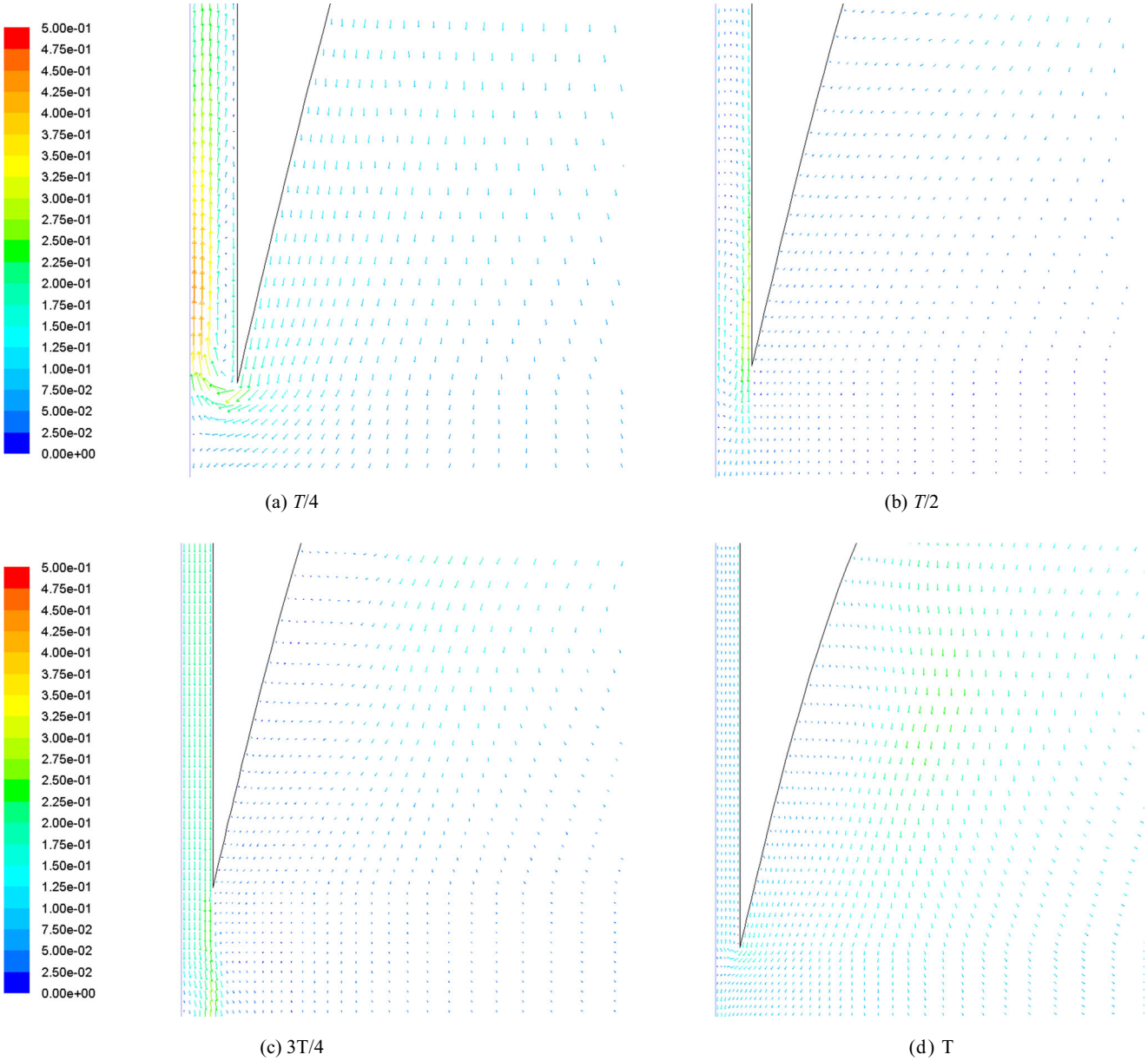

Figure 21 Velocity vectors (m/s) for test case 6 at four instances of time over one period after 30 s for the hyperbolic sine wedge

cosine components at the fundamental frequency and the first four multiples of the fundamental frequency. We determined that this is a more robust and accurate method of extracting the harmonic components than using the FFT because the FFT is sensitive to slight errors in the periodicity of the analyzed signal. As shown in Figure 23, the second and third harmonic components are significant for the Berkeley wedge profile, but all of the harmonic components are nearly constant over the test section. However, the average first harmonic A/S ratios are still consistent with the theory, as shown in Figure 16.

8 Effect of a Large Stroke on the Wave Shape for the Berkeley Wedge

Finally, we consider the effect of a large stroke on the generated wave shape. Four stroke amplitudes

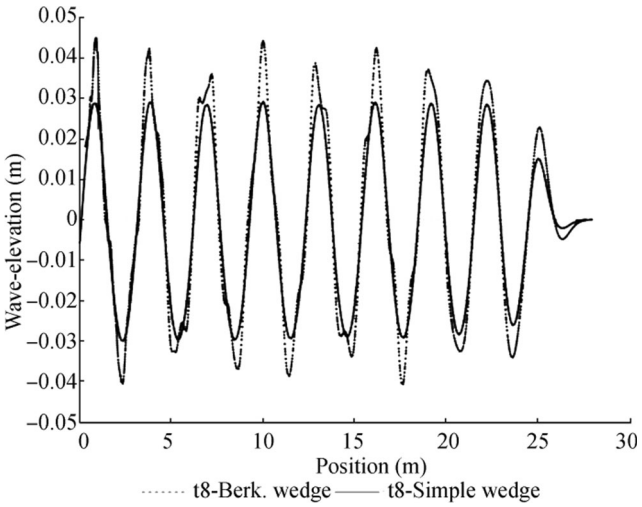

Figure 22 Comparison of the wave shapes for the Berkeley and simple wedge wave makers in test case 8

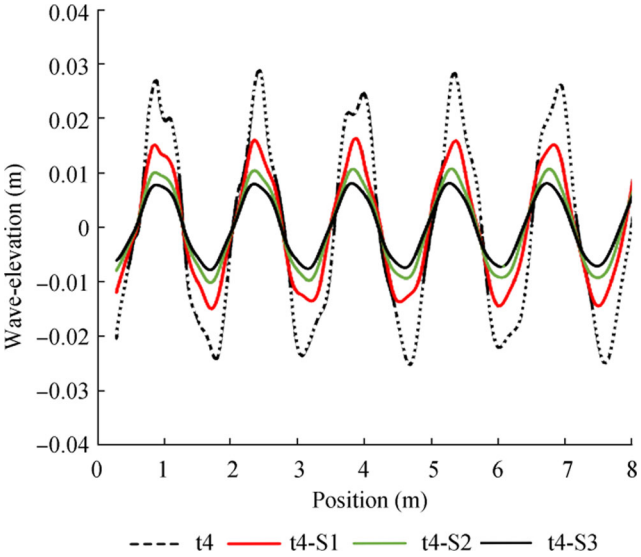

Figure 24 Wave shapes in test case 4 with lambda equal to 1.45 m and different steepness values

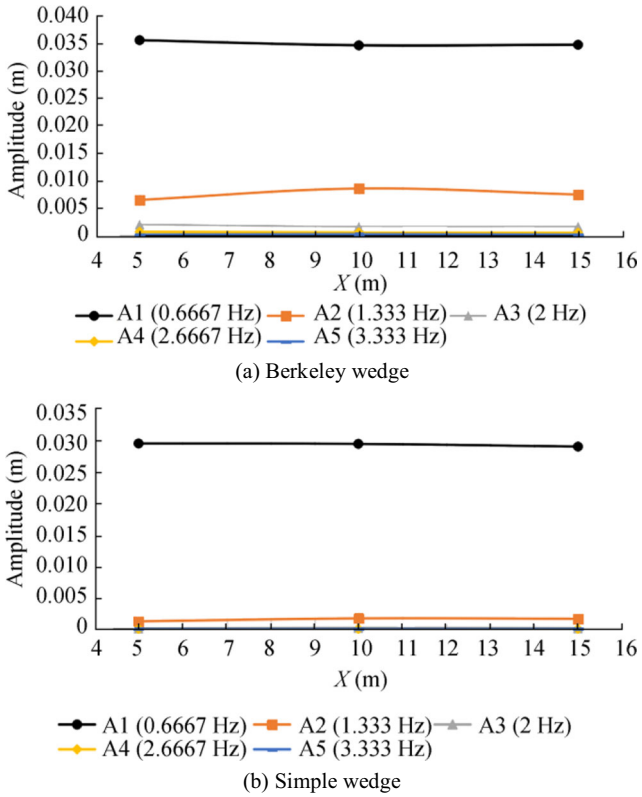

Figure 23 Comparison of the simple and Berkeley wedge harmonic components

corresponding to four different steepness values based on linear theory were applied to test case 4, as shown in Table 6. The average first harmonic *A*/*S* ratio and the average steepness of these calculations are compared with the results of linear theory, as shown in Table 6. Notably, for all stroke amplitudes, the average linear *A*/*S* ratio is consistent with the results of linear theory. Figure 24 shows the shape of the waves for each stroke, and the level of higher harmonic components increases with the wave steepness. With the decrease in the wave steepness, the wave shape tends toward a regular sinusoidal shape. However, as noted previously, the level of higher harmonic component generation tends to be larger for the Berkeley wedge than for the simple wedge, indicating that a simple wedge shape may be a better choice in practice.

Table 6 Comparison of the *A*/*S* ratio at different steepness values in test case 4 with lambda equal to 1.45 m

Test case 4	Total (m)	$\frac{H}{\lambda}$		$\frac{A}{S}$	
		Wu's theory	Present work	Wu's theory	Present work
S0	0.047	0.0342	0.0341	1.058	1.09
S1	0.028	0.02042	0.02048	1.058	1.068
S2	0.019	0.01388	0.01367	1.058	1.061
S3	0.0145	0.0105	0.0106	1.058	1.072

9 Conclusion

The ANSYS FLUENT finite-volume code is used to solve the Navier–Stokes equations for simulating the flow around a plunger-type, wedge-shaped wave maker with a gap between the wedge and the tank wall. An explicit VOF scheme is used to capture the interface in a two-phase flow. The effect of the gap on the generated wave elevation is investigated, and the smallest possible gap behind the wedge is determined to create the best quality waves.

In addition to the plane triangular wedge, two alternative profiles were tested. For the Berkeley wedge profile, good consistency with linear potential flow theory is observed for the first harmonic amplitude ratio of the far-field wave. However, for the hyperbolic sine wedge shape, high-amplitude waves are generated, which do not match the linear theory at all.

Large-amplitude motions of both the simple and Berkeley wedge profiles are also tested. The average first harmonic amplitude ratios of the waves for these cases are also consistent with the linear theory. However, higher harmonic generation is observed to increase more rapidly with increasing stroke amplitude for the Berkeley wedge than for the simple wedge, suggesting that the simple wedge may be a better choice in practice.

References

Arcari P (2015) Analysis and optimization of a wedge-type wave generator for the DTU wave. Master thesis, DTU Wind Energy, Lyngby

Azadian-Kharanjani Zohre, Nikseresht Amir H, Bingham Harry B (2018) A numerical investigation of wedge angle effects on a plunger type wave maker with a constant submerged volume. OMAE 2018-77380, V002T08A043, Madrid. Doi: https://doi.org/10.1115/OMAE2018-77380

Cengel YA, Cimbala JM (2006) Fluid mechanics: fundamentals and applications. MacGraw-Hill Companies, New York, pp 513–514

Dao MH, Chew LW, Zhang Y (2018) Modelling physical wave tank with flap paddle and porous beach in OpenFOAM. Ocean Eng 154:204–2015. https://doi.org/10.1016/j.oceaneng.2018.02.024

Elangovan M, Lal A (2008) Design and simulation of wave maker for marine industry by CFD. ANSYS India Conference (ANSYS 2008), Bangalore

Gadelho JFM, Lavrov A, Guedes Soares C (2015) CFD modelling of the waves generated by a wedge-shaped wave maker. Maritime Technology and Engineering, 993-1000. Doi: https://doi.org/10.1201/b17494-133

Hicks JBH (2017) Development and testing of optimized control signals for a plunger-type wave generator. Master thesis, DTU Mechanical Engineering, Lyngby

Higuera P, Losada IJ, Lara JL (2015) Three-dimensional numerical wave generation with moving boundaries. Coast Eng 101:35–47. https://doi.org/10.1016/j.coastaleng.2015.04.003

Kashiwagi M (1996) Full-nonlinear simulations of hydrodynamic forces on a heaving two-dimensional body. Journal of The Society of Naval Architects of Japan 180:373–381. https://doi.org/10.2534/jjasnaoe1968.1996.180_373

Keaney I, Costello R, Ringwood JV (2014) Evanescent wave reduction using a segmented wavemaker in a two dimensional wave tank. OMAE 2014-24441, V08BT06A052. Doi: https://doi.org/10.1115/OMAE2014-24441

Koo WC, Kim MH (2006) Numerical simulation of nonlinear wave and force generated by a wedge-shape wave maker. Ocean Eng 33:983–1006. https://doi.org/10.1016/j.oceaneng.2005.09.002

Lal A, Elangovan M (2008) CFD simulation and validation of plunger type wave-maker. J Math Comput Sci 2(10):708–714

Madhi F, Sinclair ME, Yeung RW (2014) The "Berkeley wedge": an asymmetrical energy-capturing floating breakwater of high performance. Marine Systems & Ocean Technology 9:5–16. https://doi.org/10.1007/BF03449282

Martínez-Ferrer PJ, Qian L, Ma Z, Causon DM, Mingham CG (2018) Improved numerical wave generation for modelling ocean and coastal engineering problems. Ocean Eng 152:257–272. https://doi.org/10.1016/j.oceaneng.2018.01.052

Mikkola T (2006) Time accurate simulation of a plunger type wave maker using unstructured finite volume solver with surface tracking. 26th Symposium on Naval Hydrodynamics, Rome

Mikkola T (2007) Simulation of plunger-type wave makers. J Struct Mech 40(4):19–39

Nikseresht AH, Alishahi MM, Emdad H (2005) Volume of fluid interface tracking with Lagrangian propagation for incompressible free surface flows. Scientia Iranica 12(2):131–140

Nikseresht AH, Alishahi MM, Emdad H (2008) Complete flow field computation around an ACV (air-cushion vehicle) using 3D VOF with Lagrangian propagation in computational domain. Comput Struct 86:627–641. https://doi.org/10.1016/j.compstruc.2007.08.006

Nikseresht AH, Alishahi MM, Emdad H (2009) Generalized curvilinear coordinate interface tracking in the computational domain. Scientia Iranica 17:64–74

Prasada DD, Ahmeda MR, Leeb YH, Sharma RN (2017) Validation of a piston type wave-maker using numerical wave tank. Ocean Eng 131:57–67. https://doi.org/10.1016/j.oceaneng.2016.12.031

Wang S (1974) Plunger-type wavemakers: theory and experiment. J Hydraul Res 12(3):357–388. https://doi.org/10.1080/00221687409499732

Wu YC (1988) Plunger-type wave-maker theory. J Hydraul Res 26(4):481–493. https://doi.org/10.1080/00221688809499206

Wu YC (1991) Waves generated by a plunger-type wavemaker. J Hydraul Res 29(6):851–860. https://doi.org/10.1080/00221689109498963

Yeung RW, Jiang Y (2014) Shape effects on viscous damping and motion of heaving cylinders. J Offshore Mech Arct Eng 136:041801-1–041801-9. https://doi.org/10.1115/1.4027650

Yim SC, Yuk D, Panizzo A, Di Risio M, Liu PLF (2008) Numerical simulations of wave generation by a vertical plunger using RANS and SPH models. J Waterw Port Coast Ocean Eng 134(3):143–159. https://doi.org/10.1061/(asce)0733-950x(2008)134:3(143)